Synthesis of the Aerodynamic Model of a Flying Wing Aircraft

Asaro, S.; Vos, Roelof

DOI
10.2514/6.2025-0852

Publication date
2025

Document Version
Final published version

Published in
Proceedings of the AIAA SCITECH 2025 Forum

Citation (APA)
Asaro, S., & Vos, R. (2025). Synthesis of the Aerodynamic Model of a Flying Wing Aircraft. In *Proceedings of the AIAA SCITECH 2025 Forum* Article AIAA 2025-0852 https://doi.org/10.2514/6.2025-0852

AIAA SciTech Forum
6-10 January 2025, Orlando, FL
AIAA SCITECH 2025 Forum

10.2514/6.2025-0852

Synthesis of the Aerodynamic Model of a Flying Wing Aircraft

Salvatore Asaro* and Roelof Vos†
Delft University of Technology, Kluyverweg 1 2629HS, Delft, The Netherlands

Flying wing aircraft, such as the Flying-V considered in this study, can substantially contribute to reducing the carbon footprint of the aviation sector. To enable adequate predictions regarding performance, stability, and control, a validated aerodynamic model of the Flying V is important. In this paper, the aerodynamic model of the Flying V is derived. The first part of the paper compares the aerodynamic coefficients determined with experiments and simulations conducted on a subscale version of the aircraft. The experiments are conducted in a wind tunnel, and with flight tests, the simulations are conducted using the vortex lattice method (VLM), panel method, and Reynolds-averaged Navier-Stokes (RANS) equations. The comparison highlights the dependency of the aerodynamic coefficients from the angle of attack, which influences the flow acting on the aircraft. Based on the outcome of the comparison for the subscale aircraft, the aerodynamic model of the full-scale aircraft is derived by combining RANS and VLM simulations. All the aerodynamic coefficients are derived as a function of the angle of attack and different Mach numbers and altitudes.

Nomenclature

b	wing span, m
$\overline{c}$	mean aerodynamic chord, m
CG	center of gravity, m
C_D, C_L	drag and lift coefficient
c_l	airfoil lift coefficient
C_x, C_y, C_z	force coefficient along X, Y, Z
C_{X_α}	force coef. along X due α
$C_{X_{\delta_e}}$	force coef. along X due δ_e
C_{Y_β}	force coef. along Y due β
C_{Y_r}	force coef. along Y due r
$C_{Y_{\delta_a}}$	force coef. along Y due δ_a
$C_{Y_{\delta_r}}$	force coef. along Y due δ_r
C_{Z_α}	force coef. along Z due α
C_{Z_q}	force coef. along Z due q
$C_{Z_{\delta_e}}$	force coef. along Z due δ_e
C_{m_x}, C_{m_y}, C_{m_z}	moment coefficient around X, Y, Z
$C_{m_{x,\beta}}$	rolling moment coef. due to β
$C_{m_{x,\delta_a}}$	rolling moment coef. due to δ_a
$C_{m_{x,\delta_r}}$	rolling moment coef. due to δ_r
$C_{m_{x,p}}$	rolling moment coef. due to $\hat{p}$
$C_{m_{x,r}}$	rolling moment coef. due to $\hat{r}$
$C_{m_{y,\alpha}}$	pitching moment coef. due to α
$C_{m_{y,\delta_e}}$	pitching moment coef. due to δ_e
$C_{m_{x,q}}$	rolling moment coef. due to $\hat{q}$
$C_{m_{z,\beta}}$	yawing moment coef. due to β
$C_{m_{z,\delta_a}}$	yawing moment coef. due to δ_a
$C_{m_{z,\delta_r}}$	yawing moment coef. due to δ_r
$C_{m_{z,p}}$	yawing moment coefficient due to $\hat{p}$
$C_{m_{z,p}}$	yawing moment coefficient due to $\hat{r}$
h	altitude, m
m	aircraft mass, kg
M_∞	freestream Mach number
p, q, r	angular velocity around X, Y, Z, m/s^2
$\hat{p}$, $\hat{q}$, $\hat{r}$	dimensionless p, q r
$Re_{\overline{c}}$	mean chord Reynolds number
S	wing reference area, m^2
U_∞	freestream velocity, m/s
X	axis and coordinate along chord direction, m
x_{hinge}	hinge line along X, m
$\mathrm{x}_{le,\overline{c}}$	mean chord leading edge along X, m
y^+	dimensionless distance from the wall
Y	axis and coordinate along span direction, m
Z	axis and coordinate along vertical direction, m
α	angle of attack, °
β	sideslip angle, °
δ_a, δ_e, δ_r	aileron, elevator, rudder deflection angle, °
ρ_∞	freestream density, kg/m^3
MTOW	Maximum take-off weight, N
MLW	Maximum landing weight, N
OEW	Operating empty weight, N
RANS, r	Reynolds-averaged Navier-Stokes
VLM, v	Vortex lattice method

---

*Postdoctoral researcher, Faculty of Aerospace Engineering, s.asaro@tudelft.nl
†Associate Professor, Faculty of Aerospace Engineering, R.Vos@tudelft.nl, AIAA Associate Fellow

I. Introduction

Tube and wing aircraft have been the standard for aviation; however, since 1990, their fuel efficiency has increased by approximately 10% while the passengers and goods transported increased 2.5 times in the same period. By 2030, if the trend continues, the aviation impact on greenhouse gas emissions will double [1]. To avoid this trend, the Advisory Council for Aeronautics Research in Europe (ACARE) with the Flightpath 2050 report aims to reduce 75% CO_2 and 90% NO_x with respect to conventional aircraft from 2000 [2]. For these reasons, integrating new technologies on aircraft is being researched to reduce the weight and footprint of future aircraft [3]. A significant reduction in aircraft emissions could also be achieved by considering new aircraft types such as Prandtl planes [4], blended wing bodies [5], flying wings [6], which could significantly increase the efficiency of the aviation sector, offering drag reduction with respect to conventional aircraft. However, because of the lack of historical statistical data, the initial design phase of an aircraft usually relies on low-fidelity tools for quickly estimating the aerodynamic model. The accuracy of these tools can be hard to estimate, particularly for unconventional aircraft. Hence, higher fidelity simulations and experiments are crucial for an adequate design, particularly to predict unanticipated non-linearities. For example, non-linearities can occur in the forces and moments due to the angle of attack α and sideslip angle β, as well as a nonlinear change in the control surfaces control authority with α and β [7]. Additionally, new aircraft could rely on different control surfaces than conventional aircraft to be controlled as leading edge fence or spoiler [8], which induce separation on the wing. Hence, low-fidelity tools cannot predict their impact on forces and moments.

The Flying-V [9], a flying-wing type aircraft, is considered in this work. An artist's impression of the Flying-V is depicted in Figure 1. The Flying-V aircraft without engines shows a maximum lift-to-drag ratio of 24.2 at cruise conditions, with an angle of attack $\alpha = 3.6°$ and freestream Mach number $M_\infty = 0.85$ [10]. Several studies have determined numerically an aerodynamic model for such aircraft [11], employing low fidelity tools such as vortex lattice and panel methods which lack the ability to predict non-linearities anticipated by wind tunnel experiments [12].

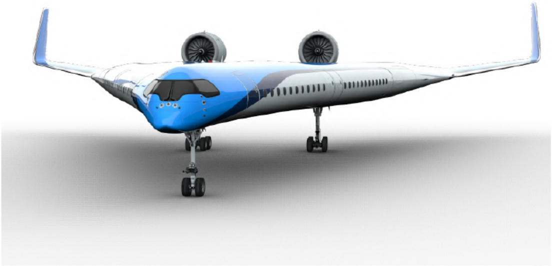

Fig. 1 Artist impression of the Flying-V aircraft

This work compares wind tunnel and flight test data with different numerical methods, such as vortex lattice method (VLM), panel method, and Reynolds-averaged Navier-Stokes (RANS) simulations. Both experimental and numerical methods are introduced in Section II. Based on the outcome of the comparison between the different methods conducted in Section III, the most suitable methods for estimating the aircraft aerodynamic model are identified. Finally, the aerodynamic model of the full-scale Flying-V is derived by combining RANS simulations and VLM simulations calibrated with the experiment in Section IV.

II. Methodology

The aerodynamic characteristics of the Flying-V are studied with several methods. Scaled versions of the aircraft are experimentally tested in the wind tunnel and with flight tests (II.A). Different fidelity methods (Section II.B) are compared with experimental results in Section III.

A. Experimental Aerodynamic Analysis

Two different types of experiments are conducted, and the models employed are depicted in Figure 2a and 2b. The former is used for flight tests and the latter for wind tunnel tests. The two models share the same geometry and dimensions, but the wind tunnel model is half the flight model. Further details on the geometry can be found in [12].

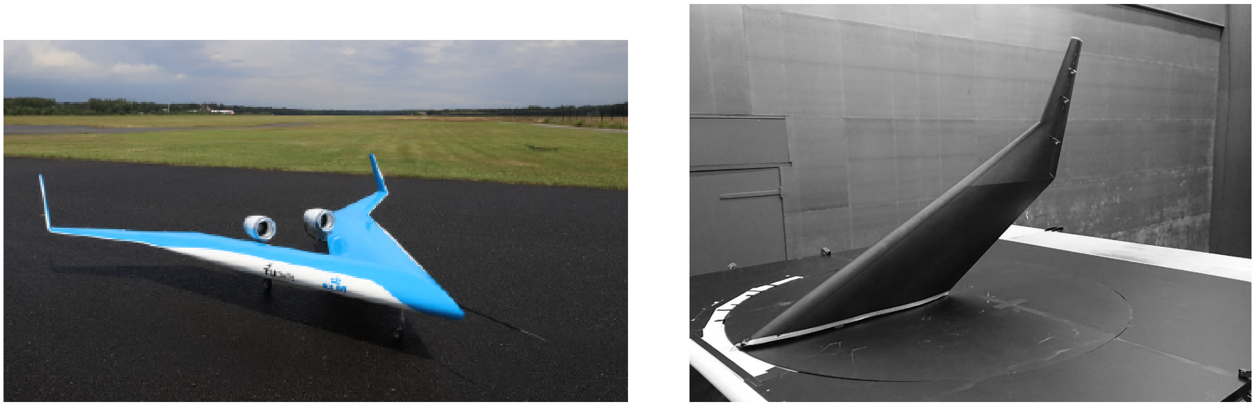

(a) Flight model [13]

(b) Wind tunnel model [12]

Fig. 2 Flight and wind tunnel models

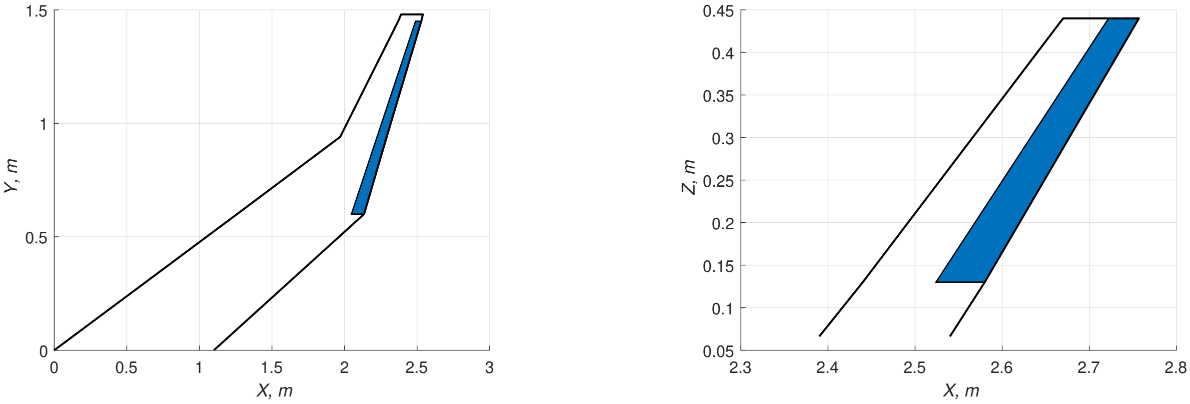

(a) Elevator/aileron on the subscale aircraft

(b) Rudder on the winglet

Fig. 3 Control surfaces on subscale aircraft

The two models also share the same control surfaces, depicted in Figures 3a and 3b. The control surface on the wing is employed as an elevator and as an aileron. The control surface on the winglet is employed as a rudder.

1. Flight tests

Flight tests are conducted with the model in Figure 2a. The model has a wing span $b = 3$ m, a wing surface $S = 1.87$ m^2 and a mean aerodynamic chord $\overline{c} = 0.81$ m, which is calculated as $\overline{c} = \frac{2}{S}\int_0^{b/2} c(y)^2 dy$. Further details on the model and the instrumentation implemented are presented in [13]. The forces and moments are calculated with respect to $0.25\overline{c}$, and the center of gravity (CG) is at $0.34\overline{c}$.

The subscale model is 4.8% of the full-scale aircraft, which is considered in Section IV; however, the two geometry are not exactly the same. The flight tests are conducted at freestream velocity U_∞ between 25-35 m/s, the angle of attack α varies in the range 0°-10° and the sideslip angle β in the range ± 5°. The model is equipped with a control surface located at the trailing edge of the outer wing, which acts as an elevator or aileron (Figure 3a), and a control surface on the winglet, acting as a rudder (Figure 3b). The control surface deflections are indicated as δ_e for elevator, δ_a for aileron and δ_r for rudder, and they are varied between $\delta_e = \delta_a = \pm 5°$, and $\delta_r = \pm 10°$. To properly operate the model during the flight tests, α, β, and the control surface angles are kept in ranges for which the forces and moments acting on the airplane are expected to change linearly.

The aircraft eigenmotions are excited with 3211 maneuvers; each maneuver activates either the elevator, the aileron, or the rudder. Further details on the tests conducted and the procedure to estimate the aerodynamic coefficient are presented in [13]. Table 1 summarizes the identified dependencies between force and moment coefficients, and angle of attack α, sideslip angle β, the control surface deflection (δ_e, δ_a, δ_r) and the dimensionless angular rates $\hat{p} = pb/(2U_\infty)$, $\hat{q} = q\overline{c}/(2U_\infty)$ and $\hat{r} = rb/(2U_\infty)$, where p, q and r are the angular rates with respect the X, Y and Z axis, respectively.

Table 1 Force and moment coefficient dependencies identified with flight tests

	α	β	$\hat{p}$	$\hat{q}$	$\hat{r}$	δ_e	δ_a	δ_r
C_X	x					x		
C_Y		x			x		x	x
C_Z	x			x		x		
C_{mx}		x	x		x		x	x
C_{my}	x			x		x		
C_{mz}		x	x		x		x	x

The flight tests allow to determine the impact of the angular rates on forces and moments, which cannot be determined otherwise with static measurements. However, as mentioned earlier, the flight tests are conducted at relatively low α, β, δ_e, δ_a, and δ_r for which forces and moments are expected to vary linearly. To study possible nonlinear effects, further tests are conducted in the wind tunnel (Section II.A.2), and the results between wind tunnel and flight tests are compared in Section III.A.

2. Wind tunnel tests

Wind tunnel experiments are conducted on the half model depicted in Figure 2b. The X-Z plane is considered a symmetry plane, i.e., the wind tunnel model has a half-span and the same mean aerodynamic chord of the subscale flight model described in Section II.A.1. The tests are carried out at $U_\infty \simeq 25$ m/s, and the temperature is kept fixed with a heat exchange, resulting in a Reynolds number calculated with the mean aerodynamic chord $Re_{\overline{c}} = 1.3{\cdot}10^6$. Forces and moments acting on the half wing are measured with a six-component balance. The balance is mounted under a turning table that varies the angle of attack α. Furthermore, the model has the same control surfaces as the subscale flight model (Section II.A.1).

The wind tunnel tests allow measuring the dependencies of force and moment from α, δ_e, δ_a, and δ_r, which can be tested at a higher range than the flight tests, allowing also to study the change of the control surface control authority with α.

B. Numerical Aerodynamic Analysis

The aerodynamic coefficient dependencies indicated in Table 1 are estimated with different fidelity tools presented herein. Numerical and experimental results are then compared in Section III, to identify the tool or combination of tools that can be employed to derive the aerodynamic model of the full scale aircraft (Section IV).

1. Vortex Lattice Method

The Vortex Lattice Method (VLM) is based on potential flow theory, i.e., the flow is incompressible and irrotational. The considered geometry, for example, a wing, is discretized with panels along the chord and the span. For each panel, a bound vortex is located at 25% chord point and a control point is located at 75% chord point, where the flow tangency condition is imposed. Each vortex induces a velocity on the other panels, calculated with the Biot-Savart law. The circulation acting on the wing is then calculated, and the linear system of equations is solved where the unknowns are the vortex circulation in each panel. The VLM does not include any viscous effect and the wing thickness. Furthermore, it cannot predict transonic flow and crossflow, which can be significant for high-swept wings. The code employed in this study is the Athena Vortex Lattice (AVL). The wing is discretized with 90 panels along the span and 30 panels along the chord. The panel distribution along the chord is finer in the leading and trailing edge areas.

2. Panel method

Similarly to VLM, the panel method is based on potential flow, where the flow is supposed to be inviscid, incompressible, and irrotational. The considered geometry is discretized with panels, and in each panel is allocated a singularity. Differently from VLM, the wing's thickness is considered by independently discretizing the upper and lower surfaces. The simulations are conducted with Flighstream. Ninety-one panels are used to discretize the aircraft along the chord direction with refinement in the leading and trailing edge area, and 90 panels are used along the span.

3. Reynolds-averaged Navier–Stokes equations

The Reynolds-averaged Navier–Stokes (RANS) simulations are solved with Ansys Fluent, which solves the equations with a finite volume method. A density-based approach is used with implicit formulation and the Monotonic Upstream-centered Scheme for Conservation Laws (MUSCL) for spatial discretization. A least-squares cell-based method with a third-order MUSCL scheme minimizes numerical diffusion. The k-ω Shear Stress Transport (k-ω SST) is employed as the turbulence model.

The meshes for the 3D RANS simulations are created with ICEM-CFD. The grids employed in this study consist of quadratic elements, and the grid is selected after a mesh independence study. The characteristics of the tested grids are summarized in Table 2. Different grids are created for the subscale and the full-scale aircraft tested in this work. However, a similar meshing strategy is followed in the two cases.

Table 2 Number of cells and y^+ used for the mesh independence study of the subscale and full scale aircraft

		Airfoil	Span	y^+	Inner	Total cells (10^6)
Subscale	Coarse	178	120	1.25	57	2.71
	Medium	224	150	1	71	5.42
	Fine	280	187	0.8	89	10.8
Full scale	Coarse	178	144	0.5	127	6.06
	Medium	224	182	0.4	156	12.1
	Fine	280	229	0.3	200	24.1

For both aircraft, three different meshes labeled Coarse, Medium, and Fine are considered with a total number of cells, which doubles. Table 2 shows the number of elements on the airfoil along the span and the region close to the aircraft, labeled inner. The inner region extends along z to a height of ca. 40% of the local chord c, as depicted in Figure 4b. The first dimensionless element height y^+ is calculated for the subscale aircraft at $M_\infty = 0.07$ and at $M_\infty = 0.85$ for the full scale aircraft. The height of the elements grows with an expansion ratio of 1.1 for both aircraft. The far-field is modeled as a semisphere with the symmetry plane coinciding with the aircraft symmetry plane. The aircraft nose is located at the center of the symmetry plane, and the semisphere has a radius of ca. $120\overline{c}$.

Table 3 summarizes the mesh independence study for the subscale aircraft. The simulations are conducted at wind tunnel conditions, i.e., $M_\infty = 0.07$ and $Re_{\overline{c}} = 1.3 \cdot 10^6$. The three grids are tested at $\alpha = 0°$, $10°$ and $20°$. The table shows the relative difference of C_D, C_L and C_{m_y} with respect to the extrapolated Richardson values, for example, $\Delta C_D = C_D - C_{D,Richardson})/C_{D,Richardson}$. The results show that the difference decreases with increasing the number of elements, as expected. Higher differences are noted for $\alpha = 0°$, where the values of the forces and moment coefficients are close to zero. For the continuation of the study, the medium mesh is used, as it will be shown in III.C, and the simulation results closely match the experimental data.

Table 4 summarizes the mesh independence study for the full-scale aircraft. The simulations are conducted at two flight conditions, i.e. $M_\infty = 0.2$ and 0.85, which corresponds to $Re_{\overline{c}} = 8.4 \cdot 10^7$ and $7.1 \cdot 10^7$, respectively. At subsonic conditions , the tested α are 0°, 10° and 20°, at transonic conditions $\alpha = 0°$, 5° and 10°. A similar trend as for the mesh independence study of the subscale aircraft can be noticed. Also, in this case, the medium mesh is selected for the continuation of the study.

Figure 4a-4b shows the medium mesh employed in this study for the subscale aircraft as an example. Figure 4a shows a plane perpendicular to the aircraft span in the location of the mean aerodynamic chord. Figure 4b shows the distribution of the elements along the chord and span.

The meshes described so far are used to study the effect of α, sideslip β, and control surfaces (elevator, aileron, and rudder) on the forces and moments acting on the aircraft. The aircraft geometry is modified to take into account

Table 3 Mesh independence study for subscale aircraft at M_∞ = 0.07 and different α, Δ is the difference with respect to Richardson extrapolation value of C_D, C_L and C_{m_y}

	α	ΔC_D	ΔC_L	ΔC_{m_y}
Coarse	0°	-0.08%	15.2%	-27.4%
	10°	-14.0%	-0.72%	14.6%
	20°	-3.9%	2.15%	6.8%
Medium	0°	-0.03%	11.2%	-19.8%
	10°	-11.7%	-0.35%	1.4%
	20°	-3.4%	1.6%	6.2%
Fine	0°	-0.01%	3.4%	-4.3%
	10°	-1.4%	-0.01%	0.02%
	20°	-0.16%	0.02%	1.7%

Table 4 Mesh independence study for full scale aircraft at M_∞ = 0.2 and M_∞ = 0.85 and different α, Δ is the difference with respect to Richardson extrapolation value of C_D, C_L and C_{m_y}

	M_∞	α	ΔC_D	ΔC_L	ΔC_{m_y}	M_∞	α	ΔC_D	ΔC_L	ΔC_{m_y}
Coarse	0.2	0°	-7.9%	-19.6%	-24.5%	0.85	0°	-28.2%	-31.2%	-36.4%
	0.2	10°	2.5%	-4.6%	-5.6%	0.85	5°	-18.0%	-4.9%	-6.2%
	0.2	20°	9.1%	-0.73%	-1.3%	0.85	10°	1.1%	-4.5%	-5.7%
Medium	0.2	0°	-2.7%	-9.9%	-12.7%	0.85	0°	-10.2%	-13.7%	-18.2%
	0.2	10°	0.1%	-1.9%	-2.4%	0.85	5°	-5.0%	-1.1%	-1.6%
	0.2	20°	6.1%	-0.005%	-0.7%	0.85	10°	1.13%	-0.37%	-0.2%
Fine	0.2	0°	-0.07%	-1.1%	-1.8%	0.85	0°	-1.3%	-2.3%	-3.9%
	0.2	10°	0.01%	-0.04%	-0.06%	0.85	5°	-0.29%	-0.01%	-0.02%
	0.2	20°	0.32%	-0.002%	-0.02%	0.85	10°	0.01%	-0.001%	-0.001%

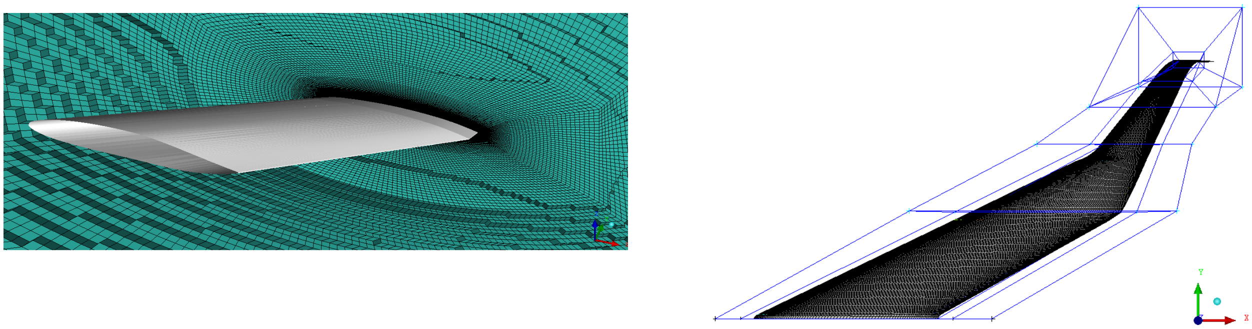

(a) Plane with mesh around the subscale aircraft for medium grid

(b) Distribution of elements on the subscale aircraft and inner block for medium grid

Fig. 4 Highlights of the mesh setup employed for the subscale aircraft, similar strategy employed for the full scale

the control surface deflection. The control surfaces are depicted in Figure 3a for the subscale aircraft and in Figure 13 for the full-scale. For simplicity, it is supposed that the control surfaces do not introduce gaps, i.e., they change smoothly the geometry. The accuracy of this hypothesis is shown in Section III, where the simulations are compared with the experimental data. The mesh software employed allows the connection of the mesh to some points along the wing. Hence, it is possible to keep the same mesh for the aircraft with and without the control surface deflection; only the inner layer is rotated to follow the aircraft geometry. The mesh described so far is mirrored with respect to the symmetry plane to simulate the sideslip angle effect, as well as the aileron and rudder.

III. Comparison of Numerical and Experimental Data

Different experimental and numerical methods are here compared for the subscale aircraft. At first, Section III.A compares wind tunnel and flight tests to identify if there are discrepancies between the two. Then, Section III compares the experimental data with different numerical methods, particularly VLM, panel method, and RANS simulations.

A. Comparison of Static Coefficients from Wind Tunnel and Flight Experiments

The aerodynamic coefficients identified with the flight tests are compared with the experiments in Figures 5a and 5b. The force and moment coefficients are divided into the two figures, allowing different scales and improving readability.

As introduced in Section II.A, the flight and the wind tunnel models share the same geometry and dimensions. However, the wind tunnel model is only half of the flight model, so the effect of the missing aileron and rudder is supposed to be superposable.

The aerodynamic coefficients considered are only the static ones, without the sideslip effect, which could not be tested in the wind tunnel. As introduced in Section II.A.1, the aerodynamic coefficients of the flight model have been identified in a previous study [13], and the error bar indicates the root mean square deviation.

For this comparison, α is limited between 0° and 15°, and the deflection of the control surfaces between ±8°. Additionally, as shown in Section III.C, the control surface authority depends on α. As the maneuvers in flight experiments are primarily conducted at $\alpha \approx 7.5°$, the coefficient shown here, for the wind tunnel experiment, is determined for the same angle of attack. The wind tunnel aerodynamic coefficients include the 95% confidence interval obtained by the polynomial fitting.

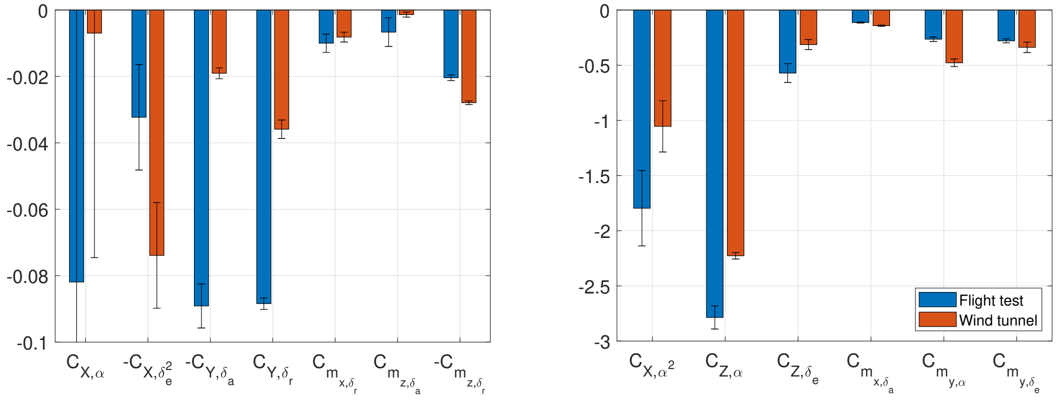

(a) Part 1

(b) Part 2

Fig. 5 Static aerodynamic coefficients from flight and wind tunnel experiments. The coefficients are grouped based on their value for easier readability

Figures 5a and 5b show that most of the coefficients predicted from the flight experiments are, in absolute value, higher than the wind tunnel ones. However, the most relevant coefficients of the three control surfaces, i.e., $C_{m_{x,\delta_a}}$, $C_{m_{y,\delta_e}}$ and $C_{m_{z,\delta_r}}$, are quite close. The coefficients dependent on α show some discrepancies, but their value from the flight experiment is not as meaningful because α cannot be varied arbitrarily. Additionally, the flight model incorporates the landing gear, the engine, and the pylon, which are not present in the wind tunnel experiment. This difference could, for example, explain the difference in $C_{m_{y,\alpha}}$.

Based on the results here presented, for the continuation of the study, the static aerodynamic coefficients to compare with the numerical simulations are extracted from the wind tunnel experiment because, as it is shown in Section III.C, the angle of attack impact all the aerodynamic coefficients.

B. Comparison of Aerodynamic Coefficients from Simulations and Experiments

The aerodynamic coefficients measured with flight and wind tunnel experiments are here compared with different numerical methods, particularly VLM, panel method, and RANS. As discussed in Section II.A, the static experimental coefficients are extracted from wind tunnel data, excluding the ones depending on β, p, q, and r, extracted from the

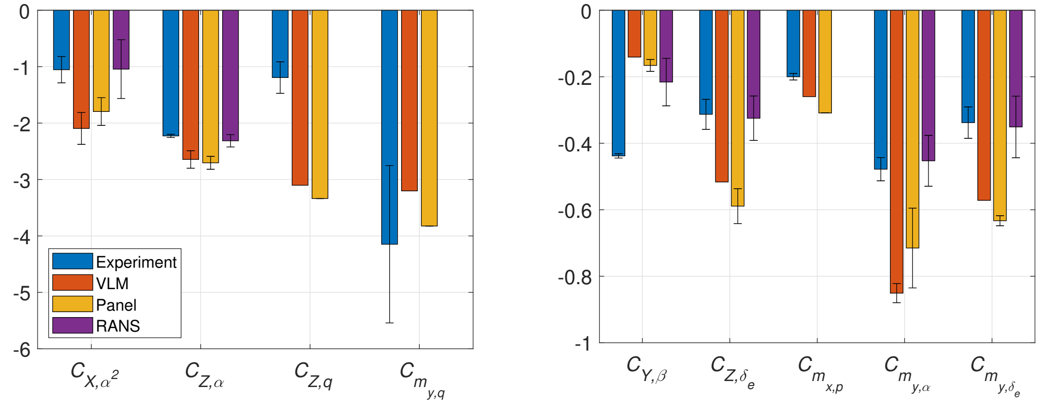

(a) Part 1 (b) Part 2

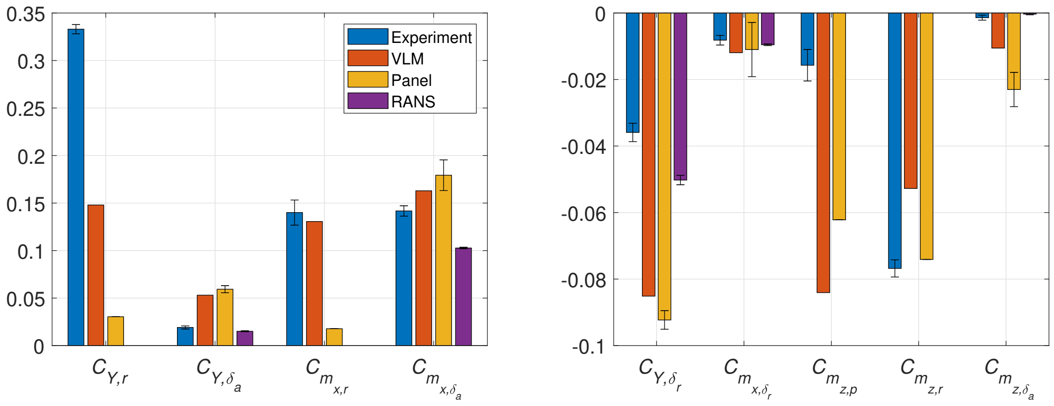

(c) Part 3 (d) Part 4

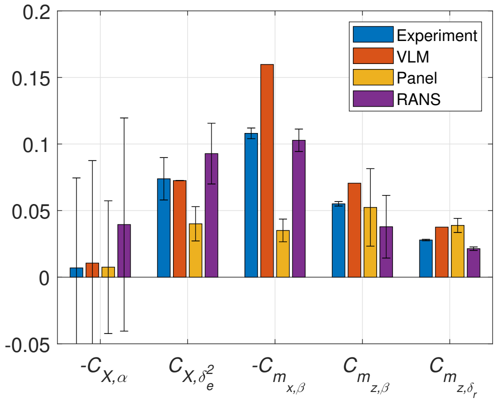

(e) Part 5

Fig. 6 Comparison of experimental and numerical aerodynamic coefficients. The coefficients are grouped based on their value for easier readability

flight experiments. The VLM and panel method feature both static and dynamic coefficients. Differently, the RANS are employed only for the static coefficients. The coefficients are estimated with a fixed $\alpha = 7.5°$ for a better comparison with the flight experiment. The effect of α is further investigated in Section III.C.

Figures 6 summarize the aerodynamic coefficients obtained using different methods. The force and moment coefficients are divided into five figures, allowing different scales and improving the readability. The coefficients obtained numerically also feature the 95% confidence interval obtained by polynomial fitting.

The aerodynamic coefficients predicted with RANS simulations are always the closest to the experimental data. The most significant difference is with $C_{Y,\beta}$. However, this coefficient is derived from the flight experiments in which the engine and the landing gear are present. Some differences are also present for $C_{m_{x,\delta_a}}$ and C_{Y,δ_r}; however, the differences are related to the considered α for this comparison. As discussed in Section III.C, the difference between RANS and experiments is lower overall when comparing the coefficients at different α.

The VLM and the Panel method show similar coefficients for ca. half of the coefficients. Overall, the VLM results are closer to experimental data, being 60% of the coefficient closer than the panel method.

For the continuation of the study in Section **??**, where the aerodynamic model is derived for the full-scale aircraft, the RANS simulations are employed for the static aerodynamic coefficients. Regarding the dynamic coefficients, the VLM is selected because it is closer to the experimental coefficients than the Panel method in 57% of the cases. Additionally, VLM is computationally less demanding than the Panel method. However, the VLM results are calibrated with the experimental data.

C. Subscale Aircraft Performance with Angle of Attack

The analysis conducted so far has considered a linear relationship between the angle of attack α and the forces and moment acting on the aircraft, and consequently, the possibility to consider the other coefficients independent from α. However, that is not always the case at higher α. This section investigates the reason for the nonlinearities by employing the RANS simulations and comparing them with experiments when possible.

Figures 7a and 7b show the relationship between drag and pitching moment coefficients as a function of the lift coefficient, respectively. The force and moment coefficients are calculated using wind tunnel measurements and RANS simulations.

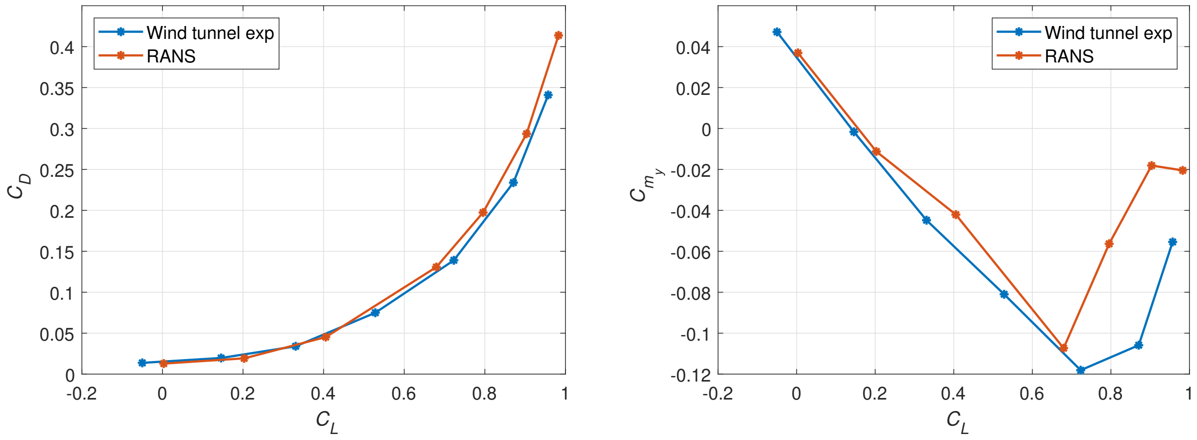

(a) Drag coefficient for subscale aircraft

(b) Pitching moment coefficient for subscale aircraft

Fig. 7 Impact of α on C_D and C_{m_y} for subscale aircraft at $M_\infty = 0.07$ and $Re_{\overline{c}} = 1.3 \cdot 10^6$

Overall, RANS simulations are able to predict the same trend as the wind tunnel experiment. Higher discrepancies can be noticed at $C_L \geq 0.6$ when the pitch break occurs. The boundary layer in the wind tunnel model is not tripped in the inner wing; however, in the RANS simulations, the flow is supposed to be fully turbulent. This difference could explain the slight discrepancies between the two datasets.

To identify the reason for the pitch break occurring at higher angles of attack, Figure 8a shows the distribution of c_Z at different locations along the span. For easier comparison, the c_Z of the airfoils along the span is divided by the C_Z of

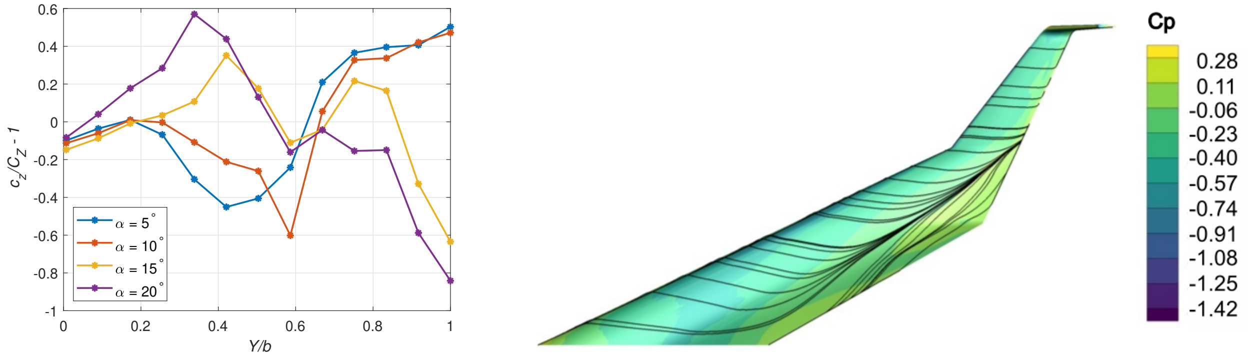

(a) $c_Z/C_Z - 1$ along the span

(b) Pressure and streamlines distribution at $\alpha = 5°$

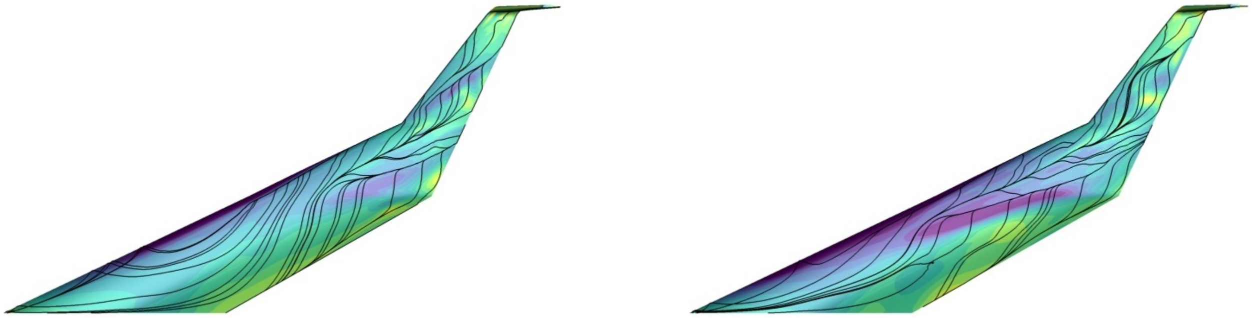

(c) Pressure and streamlines distribution at $\alpha = 15°$

(d) Pressure and streamlines distribution at $\alpha = 20°$

Fig. 8 Impact of α on C_Z along the span, and on pressure and streamlines distribution for subscale aircraft at M_∞ = 0.07 and $Re_{\overline{c}} = 1.3 \cdot 10^6$

the wing at the tested α. At lower angles of attack ($5° \leq \alpha \leq 10°$), the outer wing, which starts at $y/b = 0.63$, creates higher c_Z than the aircraft. However, with increasing α, the c_Z created by the outer wing decreases, and the c_Z created by the inner wing increases.

Figures 8b-8d depict the pressure coefficient with related streamlines on the upper wing surface at $\alpha = 5°$, 15° and 20°. In Figure 8b, the streamlines show the presence of crossflow in the trailing edge region of the inner wing, for which the pressure coefficient is close to zero or positive. In Figure 8c, at a higher angle of attack $\alpha = 15°$, but still before pitch break, it is possible to notice how the crossflow now reaches the leading edge of the wing, and there is the presence of two vortices, which show the typical S-shape in the streamlines. One vortex is located in the outer wing downstream of the leading edge kink, and one vortex is located upstream of the trailing edge kink. Both vortices lead to the formation of a suction peak on the wing, which leads, in the area where they insist, to higher c_Z than the C_Z created by the aircraft. Finally, at $\alpha = 20°$ in Figure 8d, the vortex on the inner wing has moved upstream and inboard, creating a stronger suction peak, which leads to higher c_Z in that area, differently on the outer wing the vortex has detached, and the pressure coefficient has increased, leading to smaller contribution on c_Z.

Overall, these results show how the pitch break occurs because of the crossflow in the trailing edge area, which leads to the formation of vortices that impact the lift distribution along the span. Particularly, the pitch break starts occurring when the inner wing, because of the presence of a vortex, contributes more to the total lift and hence induces a positive contribution to the pitching moment. The flow above the wing and its evolution with the angle of attack is further discussed in [14], where it is analyzed how the vortical structures would impact the flow faced by an engine located on the wing's upper surface.

Because the flow on the outer wing evolves as a function of α where the control surfaces are located, a change in the control surfaces' control authority is also expected. Figure 9a, 9b and 9c show the impact of α on $C_{m_{x,\delta_a}}$, $C_{m_{y,\delta_e}}$ and $C_{m_{z,\delta_r}}$, respectively. Each figure features wind tunnel experiment data and results of simulations conducted with VLM and RANS. Furthermore, it includes the coefficients for the flight tests used in Section III, where it was supposed that the flight tests are, on average, conducted at $\alpha \approx 7.5°$. The experiments and the simulations are conducted at $\alpha \leq 20°$,

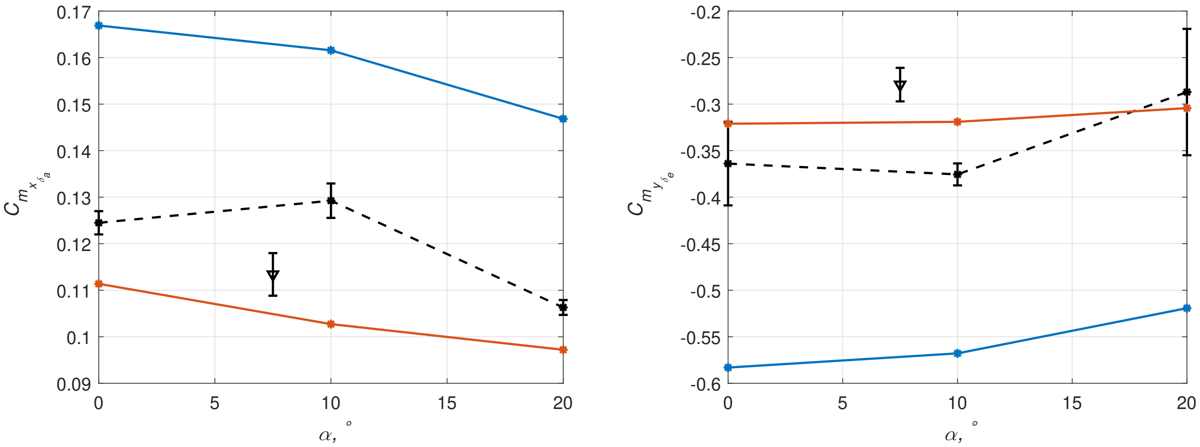

(a) Rolling moment coefficient due to aileron

(b) Pitching moment coefficient due to elevator

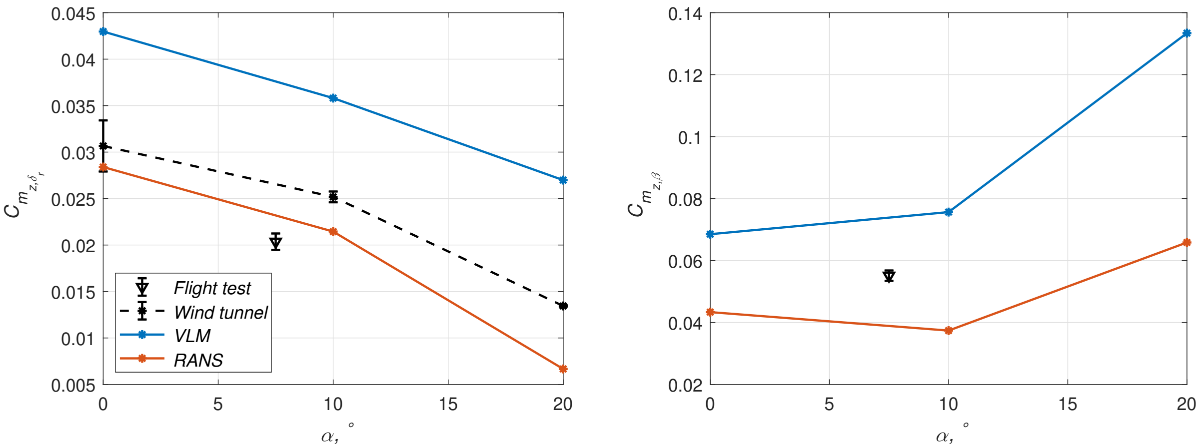

(c) Yawing moment coefficient due to rudder

(d) Yawing moment coefficient due to sideslip

Fig. 9 Impact of α on $C_{m_{x,\delta_a}}$, $C_{m_{y,\delta_e}}$ and $C_{m_{z,\delta_r}}$ for subscale aircraft at $M_\infty = 0.07$ and $Re_{\overline{c}} = 1.3 \cdot 10^6$

i.e. before the pitch break occurs.

As expected, the control authority of all the control surfaces decreases with α. For the wind tunnel experiment, $C_{m_{x,\delta_a}}$ and $C_{m_{y,\delta_e}}$ slightly increase in absolute value; however, this effect is not present in both the VLM and RANS simulations. This behavior is unclear and could be related to the laminar flow in the inner wing, which leads to a different evolution of the flow on the wing, as discussed earlier for the pitching moment. The most evident change with α occurs with $C_{m_{z,\delta_r}}$, for which the control authority is more than halved between $\alpha = 0°$ and $\alpha = 20°$. Figure 9d shows the impact of α on $C_{m_{z,\beta}}$; in this case, wind tunnel data are not available because only half model is tested. VLM predicts an increase of the coefficient with α, RANS predicts a slight decrease between $\alpha = 0°$ and $\alpha = 10°$, and then also an increase. It should be noted how the large winglet (Figure 3b) of the subscale aircraft strongly impacts the effect of the sideslip angle β.

As discussed for the other coefficients in Section III, the RANS simulations closely resemble the experimental data. The VLM can predict the trend of the change occurring with α however, the predicted coefficients are up to 50% larger in absolute value, with respect to the experimental data. The VLM is not suited to predict crossflow and vortical structures that occur on the aircraft at higher α; however, also at low α, the coefficients predicted by VLM are consistently relatively higher than the other two methods.

Overall, this section has shown how the aerodynamic coefficients depend on α, even at α lower than at the occurrence of the pitch break. However, the pitch break occurrence in terms of α, and hence of the flow on the aircraft, depends on the Mach number M_∞ as will be shown in the next section (Section IV), when considering the full-scale aircraft.

IV. Synthesis of Full Scale Aerodynamic Model

The aerodynamic model for the full-scale aircraft is derived by combining different fidelity tools. Section III.C has shown how α impacts C_{my} non-linearly and how it impacts the force and moment derivatives, for example, of the control surfaces control authority. For this reason, RANS simulations are employed to derive most of the force and moment derivatives required to describe the aircraft. VLM simulations are used to determine the dynamic force and moment derivatives as summarized in Table 5. However, the coefficients determined with VLM are calibrated with experimental data. The table indicates the dependencies of each force and moment, and they are marked with "r" if RANS simulations are employed and "v" if VLM simulations. Furthermore, each coefficient is determined at a different angle of attack α. The VLM simulations are also employed at transonic conditions. The suitability of this choice is discussed later in this section, where some results are presented.

Table 5 Force and moment coefficient dependencies, marked r when determined with RANS simulations and v with VLM simulations

	α	$\beta(\alpha)$	$\hat{p}(\alpha)$	$\hat{q}(\alpha)$	$\hat{r}(\alpha)$	$\delta_e(\alpha)$	$\delta_a(\alpha)$	$\delta_r(\alpha)$
C_X	r					r	r	r
C_Y		r			v		r	r
C_Z	r			v		r		
C_{m_x}		r	v		v		r	r
C_{m_y}	r			v		r		
C_{m_z}		r	v		v		r	r

The simulations are conducted at the flight conditions listed in Table 6. The cases are intended to describe different flight phases, i.e., take-off/landing, climb/descend, and cruise, which respectively corresponds to subsonic, high subsonic, and transonic cases.

Table 6 Flight conditions

	h, m	M_∞	ρ_∞, kg/m^3	U_∞, m/s	Re_c (10^7)
Take-off/Landing	0	0.2	1.22	68.6	8.4
	0	0.25	1.22	85.1	10.5
	0	0.3	1.22	102.1	12.6
Climb/Descend	5450	0.4	0.70	127.5	10
	7650	0.6	0.55	185.7	11.9
	9750	0.7	0.43	210.4	11
Cruise	11225	0.85	0.35	250.8	7.1

For each flight condition, the aerodynamic model is derived at different Center of Gravity (CG) values. The combination of weight and CG range are shown in Figure 10, where both the dimensional and dimensionless values are depicted in Figure 10a and 10b, respectively. The weights considered in this study are related with the FV-1000 [11], with Maximum Take-Off Weight (MTOW) of 266 tonnes. The Maximum Landing Weight (MLW) is supposed to be 76% of MTOW. The most rearward CG position of 30.1 m is located 0.5 m upstream of the neutral point; the maximum and minimum range are supposed to be 2 m and 1 m [15], respectively.

In Figure 10b, the CG is shown with respect to the leading edge location of the mean aerodynamic chord, which is calculated as $\overline{c} = \frac{2}{S}\int_0^{b/2} c(y)^2 dy$ = 18 m, with S = 898 m^2 and b = 65 m. The weights are divided with the MTOW. The moment coefficients shown hereafter are calculated with the most forward CG, i.e., CG = 28.1 m.

Herein, some highlights of the aerodynamic model are given. At first, Figure 11 shows the impact of the angle of attack α on C_L, C_D and C_{m_y}, calculated with RANS simulations. C_D and C_{my} are shown as a function of C_L in Figure

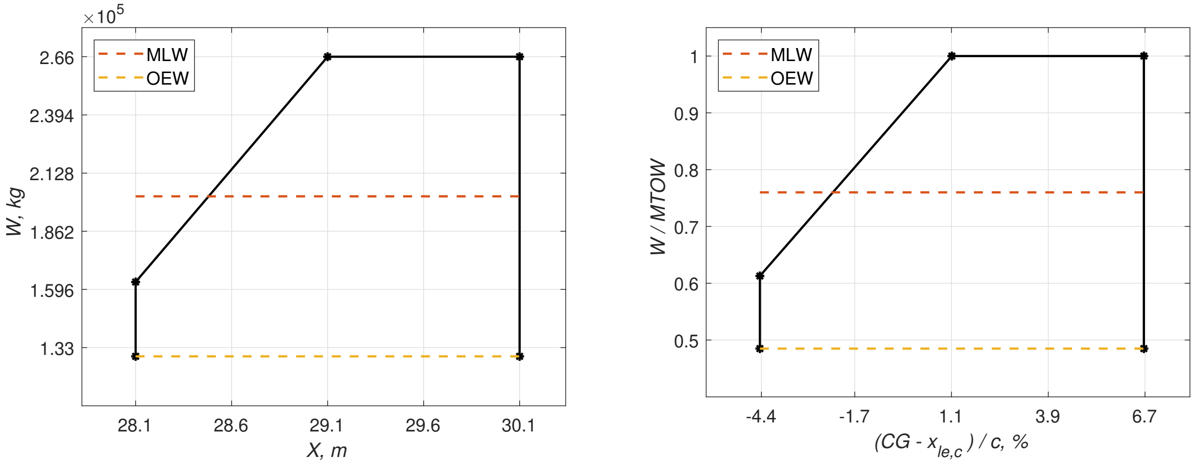

(a) Dimensional CG range and weight

(b) Dimensionless CG range and weight

Fig. 10 Dimensional and dimensionless Center of Gravity (CG) and aircraft weight with $\overline{c}$ = 18 m

11a and 11b, respectively. Starting from Figure 11b, it is evident that the pitch break occurs at lower α or C_L, increasing the M_∞. The cause of the pitch break has been discussed in Section III.C. At the same C_L for which pitch break starts, it is possible to see a change in slope in Figure 11a, particularly the C_D is higher than it would be by extrapolating from lower C_L. The pitch break limits the available maximum C_L; however, as shown in [16], it is possible to trim the aircraft at the considered operating conditions and perform maneuvers. A critical point would be disturbances occurring during flight, such as gusts, which could lead to a change in α for which $C_{m_{y,\alpha}} > 0$. It is likely necessary to modify the wing or add fences, which could postpone the occurrence of the pitch break at higher C_L.

The effect of the angle of attack α and the Mach number M_∞ are now considered for different aerodynamic coefficients. The figure herein presented includes, as error bars, the 95% confidence interval of the linear fitting to determine the coefficients. A high confidence interval indicates lower linearity between the moments and the variable which induces them. For this reason, the aerodynamic model is used as a look-up table; however, it is preferred to estimate the coefficients to highlight some general trends here.

Figures 12a and 12b show the impact of α and M_∞ on $C_{m_{x,\beta}}$ and $C_{m_{z,\beta}}$, respectively. The sideslip angles considered

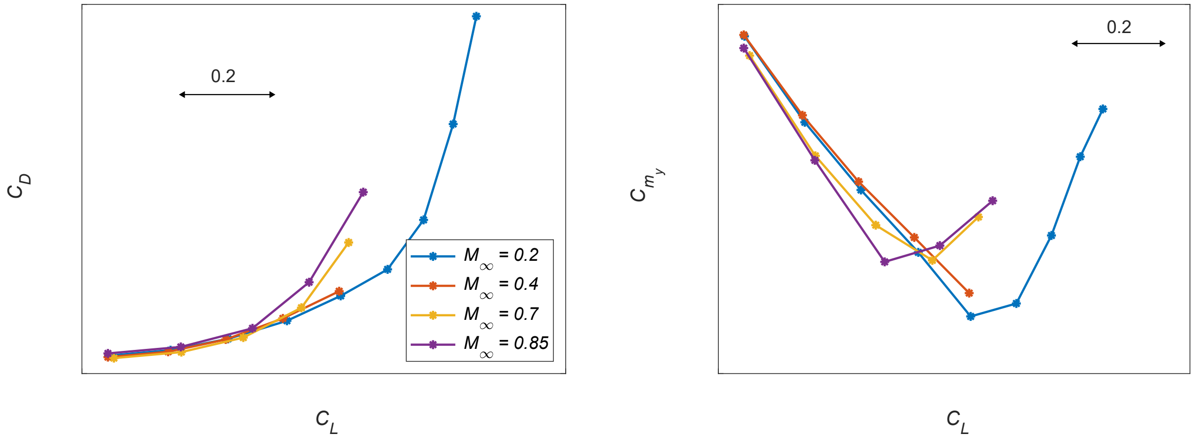

(a) Drag coefficient

(b) Pitching moment coefficient

Fig. 11 Impact of α on C_L, C_D and C_{m_y} at different operating conditions

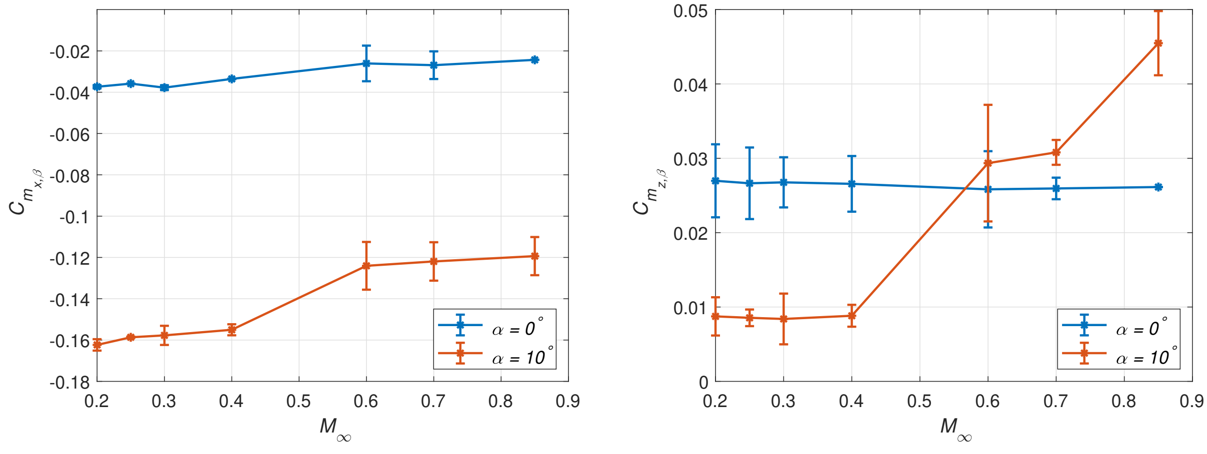

(a) $M_\infty - C_{m_{x,\beta}}$

(b) $M_\infty - C_{m_{z,\beta}}$

Fig. 12 Impact of M_∞ on $C_{m_{x,\beta}}$ and $C_{m_{z,\beta}}$ at different angles of attack

are β = 7.5° and 15°. The results clearly highlight that considering the effect of β not dependent from α, i.e., supposing superposition of the two effects can lead to substantial differences. A similar trend has been observed in Section III.C; however, because the occurrence of the pitch break varies with α at different M_∞, it is also not sufficient to consider the effect occurring at subsonic speeds also for the high subsonic/transonic cases. The reason for this is clear by observing the evolutions of the coefficients in Figures 12a and 12b as a function of M_∞. The coefficients are similar between each other for $M_\infty \leq 0.4$ and $M_\infty > 0.4$, but there are clear differences between the two groups, i.e., subsonic cases and high subsonic/transonic cases.

A big impact of M_∞ at $\alpha = 10°$ can be observed in Figure 12b, where $C_{m_{z,\beta}}$ increases almost linearly with $M_\infty > 0.6$. The shock present at these flight conditions leads to a different development of the vortical structure occurring at α = 10° on the left and right side of the aircraft, leading to the observed change in moment coefficients.

Figure 13 depicts the control surfaces simulated with RANS simulations. Particularly, Figure 13a shows a control surface on the inner wing, which would act as a high lift device, and the control surface on the outer wing, which is used as an elevator and as an aileron. Figure 13b shows the rudder on the winglet. The simulations with the aileron and

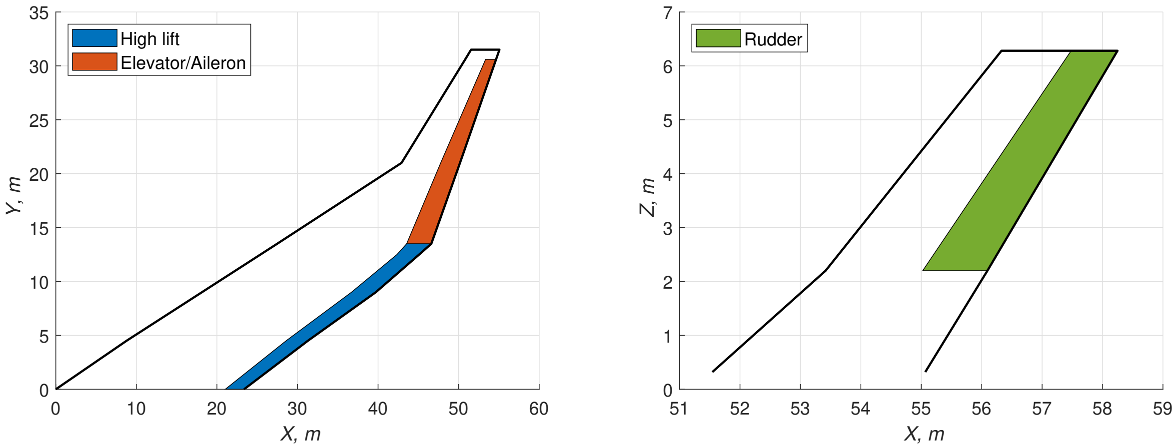

(a) High lift, aileron and elevator on the wing

(b) Rudder on the winglet

Fig. 13 Control surfaces simulated with RANS. Their dimension and distribution do not reflect the final layout

rudder are conducted by mirroring the geometry with respect to the symmetry plane. The control surfaces depicted here are not intended to be the final ones to be implemented on the aircraft. In [16], the aerodynamic coefficients obtained with the RANS simulations here presented are used to calibrate VLM results, so to be able to take into account the effect of α and M_∞, but also to be able to more rapidly assess different control surfaces layout which can allow maneuverability of the aircraft at all flight conditions and hence the ability to comply with the certification requirements.

The effect of M_∞ and α on $C_{m_{x,\delta_a}}$, $C_{m_{y,\delta_e}}$ and $C_{m_{z,\delta_r}}$ are shown in Figure 14a, 14b and 14c, respectively. The control surface deflections used to calculate the coefficients are δ_a = -30°:15°:30°, δ_e = -30°:15°:0° and δ_r = -30°:15°:30°. For both the aileron and rudder, the surfaces on the left and right sides of the wing are deflected at the same angle; for the aileron, one side is deflected upward and one side downward. The figures include, as error bars, the 95% confidence interval of the linear fitting to determine the coefficients.

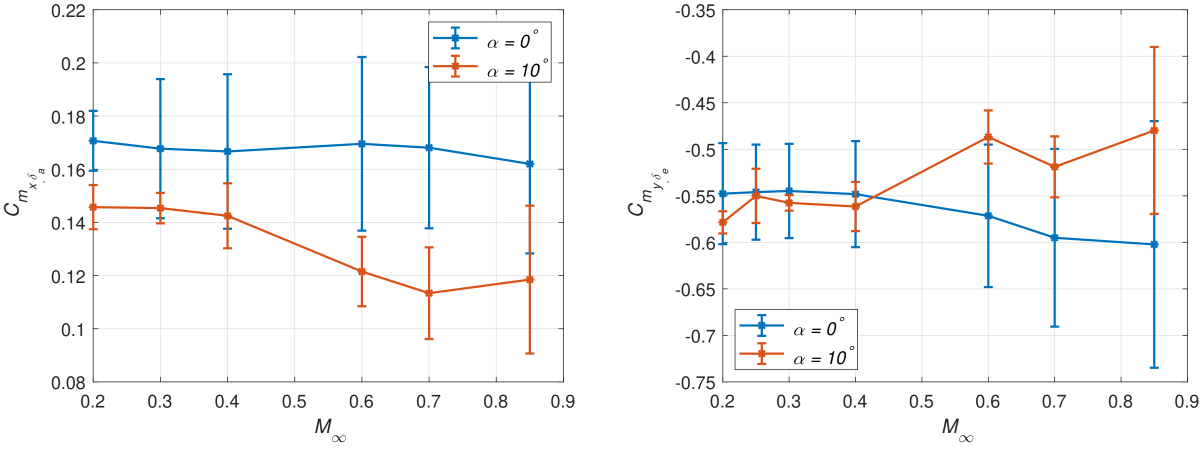

(a) Rolling moment due to aileron deflection

(b) Pitching moment due to elevator deflection

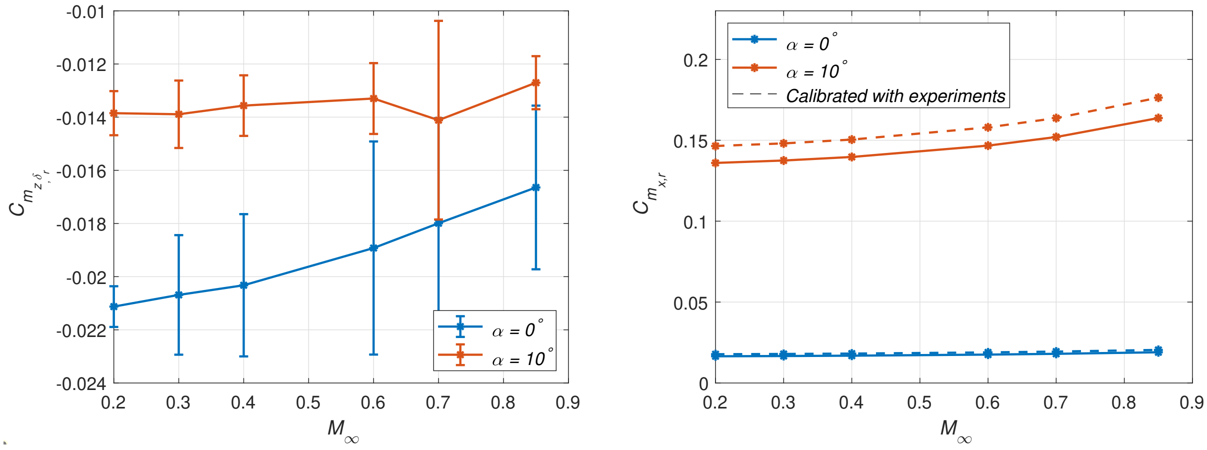

(c) Yawing moment due to rudder deflection

(d) Rolling moment due to yaw rate, calibrated with the subscale flight experiment

Fig. 14 Impact of M_∞ on the moment derivatives $C_{m_{x,\delta_a}}$, $C_{m_{y,\delta_e}}$, $C_{m_{z,\delta_r}}$ and $C_{m_{z,p}}$ due to, respectively, aileron, elevator, rudder and $\hat{r}$

In Figure 14a, $C_{m_{x,\delta_a}}$ tends to decrease with α and also with M_∞. The impact is particularly evident for α = 10° and high subsonic/transonic cases. Figure 12a had shown that the requirement of $C_{m_{x,\beta}}$ would increase with α. Hence, there can be high aileron requirements to compensate for the sideslip.

In Figure 14b, $C_{m_{y,\delta_e}}$ increases with M_∞ at α = 0° but it has the opposite trend at α = 10°. The different trends lead to having slightly higher control authority of the elevator at α = 10° and $M_\infty \leq 0.4$ with respect to α = 0°, and the opposite behavior for $M_\infty > 0.4$.

In Figure 14c, the control authority of the rudder $C_{m_{z,\delta_r}}$ significantly decreases with α. Generally $C_{m_{z,\delta_r}}$ decreases also with M_∞. However, the decrease is higher at $\alpha = 0°$ than at $10°$, leading to a smaller decrease of the control authority of the rudder at a higher speed.

Figure 14d depicts the evolution of $C_{m_{x,r}}$ showing an increase, in absolute value, with M_∞, dictated by the Prandtl–Glauert correction and a significant increase with α. The VLM code should not be able to predict the dynamic derivative at α for which separation occurs [7]. However, as observed in Section III.C, the VLM could predict the change but not the absolute value of the aerodynamic coefficients as a function of α before the occurrence of the pitch break. The aircraft cannot fly for α higher than the pitch break, so the change with α with VLM is here deemed adequate, but the VLM results are calibrated with the dynamic coefficients obtained with the flight tests and presented in Section III. The M_∞ effect, based on previous studies as [17], should not significantly impact the coefficients. Unsteady RANS simulations can also be performed to determine the aerodynamic dynamic coefficients as in [18]-[19], showing a limited impact of M_∞ in the flight conditions considered herein.

Overall, these results have shown that the effect of α on the control surface control authority is not straightforward, and hence, supposing the superposition of the effects would significantly impact the results. Furthermore, the evolution of the coefficients with M_∞ is, for most cases, opposite of what the Prandtl–Glauert correction would predict, i.e., the control authority decreases with M_∞.

The aerodynamic model of the full-scale aircraft is here determined at different angles of attack, Mach numbers, and altitudes by combining RANS and VLM simulations. Particularly, RANS are employed to determine the static aerodynamic coefficients, and VLM is calibrated with experiments for the dynamic aerodynamic coefficients.

V. Conclusion

The present work proposed an aerodynamic model for a flying wing aircraft. The aerodynamic coefficients are derived with a combination of Reynolds-Averaged Navier-Stokes (RANS) simulations for the static coefficients and Vortex Lattice Method (VLM) simulations calibrated with experiment for the dynamic coefficients.

Different experimental and numerical methods are initially compared for a subscale version of the Flying-V. The experiments comprise wind tunnel and flight data, and the two data sets are compared and combined for further comparison with numerical methods. Particularly, the static coefficients are extracted from the wind tunnel data, and the dynamic coefficients are extracted from the flight data. The experimental data are then compared with VLM, panel method, and RANS simulations. The RANS simulations are used only for the static coefficients. The comparison shows that the RANS more closely resemble the experimental static coefficients and the VLM the dynamic ones. Further comparison between numerical and experimental methods shows how the occurrence of a pitch break in the $C_{m_{y,\alpha}}$ curve can be adequately predicted by RANS, as well as the consequent impact of α on the control surface control authority.

Based on the comparison, the aerodynamic model for the full-scale aircraft is determined by combining RANS simulations and VLM calibrated with the experiment, with the former for the static coefficients and the latter for dynamic coefficients. The simulations are conducted at different Mach numbers M_∞ and altitudes. Furthermore, each coefficient is also simulated at different α.

Acknowledgments

This publication is part of the project Flying V Flight Control with project number 19511 of the research program Open Technology Programme, which is (partly) financed by the Dutch Research Council (NWO). The authors would like to acknowledge the in-kind contribution of KLM Royal Dutch Airlines and ADSE. Furthermore, the authors would like to thank Malcom Brown for his help with the wind tunnel experiment.

References

[1] Miller, J. D., and Façanha, C., "The state of clean trnasport policy - a 2014 synthesis of vehicle and fuel policy developments," Tech. rep., The International Council on Clean Transportation, 2014.

[2] Darecki, M., Edelstenne, C., Enders, T., et al., "Flightpath 2050 - Europe's Vision for Aviation," Tech. Rep. EUR 098 EN, European Commission, 2011.

[3] Mosca, V., Karpuk, S., Sudhi, A., Badrya, C., and Elham, A., "Multidisciplinary design optimisation of a fully electric

regional aircraft wing with active flow control technology," *The Aeronautical Journal*, Vol. 126, No. 1298, 2022, p. 730–754. https://doi.org/10.1017/aer.2021.101.

[4] Frediani, A., Cipolla, V., and Rizzo, E., "The PrandtlPlane Configuration: Overview on Possible Applications to Civil Aviation," *Variational Analysis and Aerospace Engineering: Mathematical Challenges for Aerospace Design*, Boston, United States of America, 2012. https://doi.org/10.1007/978-1-4614-2435-2_8.

[5] Liebeck, R. H., "Design of the Blended Wing Body Subsonic Transport," *Journal of Aircraft*, Vol. 41, No. 1, 2012, pp. 10–25. https://doi.org/10.2514/1.9084.

[6] Martínez-Val, R., Pérez, E., Alfaro, P., and Pérez, J., "Conceptual design of a medium size flying wing," *Proceedings of the Institution of Mechanical Engineers, Part G: Journal of Aerospace Engineering*, Vol. 221, 2007, pp. 57–66. https://doi.org/10.1243/09544100JAERO90.

[7] Park, J., Choi, J.-Y., Jo, Y., and Choi, S., "Stability and Control of Tailless Aircraft Using Variable-Fidelity Aerodynamic Analysis," *Journal of Aircraft*, Vol. 54, No. 6, November–December 2017, pp. 2148–2164. https://doi.org/10.2514/1.C034052.

[8] Paul, M., and Rein, M., "Transonic Numerical and Experimental Evaluation of Unconventional Lambda Wing Control Surfaces," *Journal of Aircraft*, Vol. 54, No. 3, 2017, pp. 1139–1149. https://doi.org/10.2514/1.C034080.

[9] Benad, J., "The Flying V - A new aircraft configuration for commercial passenger transport," *Deutscher Luft-und Raumfahrtkongress*, Rostock, Germany, 2015. https://doi.org/10.25967/370094.

[10] Laar, Y., Atherstone, D., Benad, J., and Vos, R., "Aerodynamic Design of a Flying V Aircraft in Transonic Conditions," *AIAA SciTech*, Orlando, United States of America, January 2024.

[11] Oosterom, W., and Vos, R., "Conceptual Design of a Flying-V Aircraft Family," *AIAA SciTech*, Virtual event, January 2021. https://doi.org/10.2514/6.2021-0874.

[12] Palermo, M., and Vos, R., "Experimental Aerodynamic Analysis of a 4.6%-Scale Flying-V Subsonic Transport," *AIAA SciTech*, Orlando, United States of America, 2020. https://doi.org/10.2514/6.2022-0713.

[13] García, A. R., Brown, M., Atherstone, D., van Arnhem, N., and Vos, R., "Aerodynamic Model Identification of the Flying V from Sub-Scale Flight Test Data," *AIAA SciTech*, San Diego, United States of America, 2022. https://doi.org/10.2514/6.2022-0713.

[14] Kumar, A., Asaro, S., and Vos, R., "Aerodynamic Analysis of the Flying V Subsonic Transport to Enable Engine Integration," *AIAA SciTech*, Orlando, United States of America, 2025.

[15] van der Toorn, M., "Flying-V Family - Design for Stability and Control," Master thesis, Technische Universiteit Delft, 2022.

[16] Asaro, S., Atmaca, D., van Kampen, E.-J., and Vos, R., "Control Surface Allocation based on Offline Handling Quality Simulations for a Flying Wing Aircraft," *AIAA SciTech*, Orlando, United States of America, 2025.

[17] Winchenbach, G. L., Uselton, B. L., Vathaway, W. H., and Chelekis, L. R., "Comparison of Free-Flig ht and Wind Tunnel Data for a Generic Fighter Configuration," *AIAA 9th Atmospheric Flight Mechanics Conference*, San Diego, United States of America, 1982.

[18] Ghoreyshi, M., and Cummings, R. M., "Unsteady aerodynamics modeling for aircraft maneuvers: A new approach using time-dependent surrogate modeling," *Aerospace Science and Technology*, Vol. 39, 2014, p. 222–242. https://doi.org/10.1016/j.ast.2014.09.009.

[19] Da Ronch, A., Ghoreyshi, M., Badcock, K., and Vallespin, D., "Computation of Dynamic Derivatives Using CFD," *28th AIAA Applied Aerodynamics Conference*, Chicago, United States of America, 2010. https://doi.org/10.2514/6.2010-4817.